

# The Carnegie RR Lyrae Program: The Mid-Infrared RR Lyrae Period-Luminosity Relation in $\omega$ Cen and also metallicity [working title]

Meredith J. Durbin<sup>1,2\*</sup> Victoria Scowcroft<sup>3</sup> Wendy L. Freedman<sup>4</sup> Barry F. Madore<sup>3</sup>  
 Rachael L. Beaton<sup>3</sup> Andrew J. Monson<sup>5</sup> Mark Seibert<sup>3</sup>

<sup>1</sup> *Space Telescope Science Institute, 3700 San Martin Drive, Baltimore, MD 21218, USA*

<sup>2</sup> *Pomona College, Claremont, CA 91711, USA*

<sup>3</sup> *Observatories of the Carnegie Institution of Washington, 813 Santa Barbara St., Pasadena, CA 91101, USA*

<sup>4</sup> *Department of Astronomy and Astrophysics, University of Chicago, 5640 S Ellis Ave, Chicago, IL 60637, USA*

<sup>5</sup> *Department of Astronomy and Astrophysics, The Pennsylvania State University, 403 Davey Lab, University Park, PA, 16802, USA*

Accepted XXX. Received YYY; in original form ZZZ

## ABSTRACT

[abstract]

**Key words:** keyword1 - keyword2 - keyword3

## 1 INTRODUCTION

The Carnegie RR Lyrae Program (CRRP) is a Warm *Spitzer* program (Freedman et al. 2012a, PID 90002) with the aim of calibrating the mid-infrared (mid-IR) RR Lyrae period-luminosity (PL) relation. Similar to the Carnegie Hubble Program (CHP) (Freedman et al. 2011), which used mid-IR observations of Cepheids to measure the Hubble constant ( $H_0$  Freedman et al. 2012b), the results of the CRRP will be used to provide an independent, population II calibration of the zero-point of the extragalactic distance scale, and hence an independent measurement of  $H_0$ .

In recent years it has become increasingly important to obtain independent direct measurements of  $H_0$ . The results of Riess et al. (2011) and Freedman et al. (2012b), both which use Cepheids and type Ia supernovae (SNe), agree very well at  $74.4 \pm 2.5$  km s<sup>−1</sup> Mpc<sup>−1</sup> and  $74.3 \pm 2.6$  km s<sup>−1</sup> Mpc<sup>−1</sup>, respectively. However, when we consider the latest results from *Planck*, who find  $67.48 \pm 0.98$  km s<sup>−1</sup> Mpc<sup>−1</sup> (Planck Collaboration et al. 2015), there is tension. The *Planck* study derives its measurement from a model of the cosmic microwave background (CMB), so is completely independent of the Riess et al. and Freedman et al. results.

There have been several recent works that have investigated possible sources of uncertainty in the distance ladder that may contribute to the discrepancy between  $H_0$  measurements. For example, Rigault et al. (2015) examine the differences in star formation rates in type Ia SNe host galaxies. They find that the intrinsic brightness of a SNe Ia may

be affected by the local host environment; i.e. whether the SN occurs in a locally star forming or locally passive environment. Efstathiou (2014) reanalysed the Cepheid data from Riess et al. (2011), and found that the outlier rejection criteria in their analysis of NGC4258 lowered the resultant value of  $H_0$  to  $70.6 \pm 3.3$  km s<sup>−1</sup> Mpc<sup>−1</sup>, making it compatible with the value from *Planck*.

The CRRP assesses a systematic that was unreachable in the original CHP – the intrinsic accuracy of the mid-IR Cepheid standard candle distance scale when compared to the standard ruler distance scale of the CMB and Baryon Acoustic Oscillation (BAO) measurements. With only one “test candle” it was impossible to make any assessment of this accuracy. However, with two standard candles with similar precision we can make meaningful comparisons and assess their systematic accuracy.

RR Lyrae variables (hereafter RRL) are intrinsically fainter than Cepheids, and in the optical follow a much shallower, even horizontal, PL relation (Catelan et al. 2004). Determining an accurate distance to an RRL in the *V* band requires knowledge of its metallicity. However, Longmore et al. (1986) showed that the true power of RRL as distance indicators lies in the IR passbands. Recently, several groups have been studying the populations of RRL in globular clusters and nearby dwarf spheroidal galaxies in the infrared (e.g. Garofalo et al. 2013; Ordoñez et al. 2014; Cusano et al. 2015; Kains et al. 2015, and references therein). Several Galactic RRL now have high precision geometric distances measured as part of the HST-fine guidance sensor (HST-FGS) parallax program (Benedict et al. 2011) [FIND REF], and can be used to calibrate the absolute zero-point of the RRL PL relation.

\* E-mail: mdurbin@stsci.edu

Distance measurements made in the mid-IR benefit from reduced extinction effects, where  $A_{[3.6]}$  and  $A_{[4.5]}$  are 16 to 20 times lower than  $A_V$  (Cardelli et al. 1989; Indebetouw et al. 2005). Additionally, the precision of distances obtained from the RRL PL relation is increased. At the wavelengths observed by Warm *Spitzer* (3.6 and 4.5  $\mu\text{m}$ ) we do not see photospheric effects, but only the effects of temperature driving the pulsation; essentially, the mid-infrared light curve is tracing the change in radius of the star through the pulsation cycle. A by-product of this effect is that the intrinsic width of the RRL PL relation is also minimised in the mid-IR. The PL relation for pulsational variables can be thought of as a two-dimensional projection of the three-dimensional period-luminosity-colour relation (see figure 3 of Madore & Freedman (1991) for a graphical representation). As the effects of temperature are reduced, the colour-width of the PL decreases in the mid-IR. As one moves from the optical to the mid-IR, the slope of the PL relation steepens and its dispersion dramatically decreases, and the slope should asymptotically approach the predicted slope of the period-radius relation, resulting in a slope between  $-2.4$  and  $-2.8$ , confirmed empirically by Madore et al. (2013). Through this decrease in dispersion we have found that the intrinsic width of the mid-IR PL for RRL is in fact *smaller* than for Cepheids – less than 0.05 mag compared to 0.10 mag (Neeley et al. 2015). This translates to an uncertainty on an individual RRL of below 2%, compared to 4% for Cepheids. Thus, for nearby systems RRL are the most precise standard candles.

In this work we focus on the effects of metallicity on the RRL PL relation in the mid-infrared. Several Galactic Globular Clusters are being observed as part of CRRP, but  $\omega$  Cen is unique in that it exhibits a measureable spread in metallicity (Freeman & Rodgers 1975; Villanova et al. 2007, 2014).

There are very few metallic or molecular transition lines in the mid-IR at typical RRL temperatures, so the effects of metallicity on luminosity should be minimised. However,  $\omega$  Cen provides the ideal test bed for any effect that we may not have predicted. Such an effect is not out of the realm of possibility; for example, the strength of the CO band head at 4.5  $\mu\text{m}$  has been found to have a significant effect on Cepheid colours Marengo et al. (2010) [FIND REF], and has such prevented the IRAC 4.5  $\mu\text{m}$  Cepheid observations from being used for distance measurements in the CHP (Scowcroft et al. 2011; Monson et al. 2012; Scowcroft et al. 2016). As our concern in this program is systematic precision, we must ensure that similar effects do not plague the RRL distance scale.

The paper is set out as follows: Section 2 details the observations and data reduction. Section 3 presents the photometry of the  $\omega$  Cen RRL. Section 4 describes the mid-IR PL relations and Section 5 discusses the application of these to a distance measurement of  $\omega$  Cen. Section 6 examines the effects of metallicity on RRL magnitudes and distance estimates. Section 7 discusses the implications of this, and other systematic effects we consider in this work. In Section 8 we present our conclusions.

## 2 OBSERVATIONS & DATA REDUCTION

This work combines mid-IR observations from the Warm *Spitzer* mission, with supporting near-IR observations from the FourStar instrument on the Baade-Magellan telescope at Las Campanas Observatory (Persson et al. 2013). Figure 1 shows a  $K_s$  FourStar image with the *Spitzer* fields outlined, the positions of known RRab plotted as circles, and the positions of known RRC as triangles.

### 2.1 Warm *Spitzer* Data

The Warm *Spitzer* observations for this work were taken as part of the CRRP. Three fields in  $\omega$  Cen were chosen; their positions and the positions of known  $\omega$  Cen RRLs are shown in Figure 1. To obtain optimal RRL light curves we observed each field 12 times over approximately 16 hours, roughly corresponding to the period of the longest period RRL we expected in the field. The observations of all three fields were taken on 2013 May 10 and 2013 May 11. Each field was observed using *Spitzer* IRAC (Fazio et al. 2004) with a 30s frame time with a medium scale, gaussian 5-point dither pattern to mitigate any image artefacts. Images were collected in both the 3.6 and 4.5  $\mu\text{m}$  channels. The elongated field shapes come from the design of IRAC; while the [3.6] channel is collecting on-target data, the [4.5] channel collects off target data “for free”, and vice versa. We chose to include these off-target fields to maximise the number of RRL in our final sample and to increase the legacy value of our data set to the community.

The science images were created using MOPEX (Makovoz et al. 2006), first running overlap correction on the corrected basic calibrated data frames (cBCDs) then mosaicking them at 0.6 arcsec pixel scale using the drizzle algorithm. Mosaicked location-correction images were created at the same time.

PSF photometry was performed using DAOPHOT and ALLFRAME (Stetson 1987, 1994). The PSF model was created for each field/filter combination using the first epoch data. This was then applied to each other epoch. As the observations were taken temporally close together the effects of telescope rotation between epochs on the mosaicked PSF were minimal, so making a single good PSF model for each field/filter combination was much more efficient than creating one for every epoch.

Master star lists for ALLFRAME were created for each filter/field combination using a median mosaicked image created by MOPEX. We did not use the same single master star list for both filters as only a small proportion (1/3) of the 3.6  $\mu\text{m}$  and 4.5  $\mu\text{m}$  fields overlap each other. Instead we performed separate ALLFRAME reductions for each filter, and combined the results after the fact using DAOMATCH and DAOMASTER. Our mid-IR photometry is calibrated to the standard system set by Reach et al. (2005).

### 2.2 FourStar Data

$J$ ,  $H$  and  $K_s$  data were taken with the FourStar instrument on the Baade-Magellan telescope at Las Campanas Observatory (Persson et al. 2013) on the nights of 2013 June 25, 2013 June 27, and 2013 June 28. Four epochs were obtained each night in each filter for a total of 12 epochs. A mosaic of

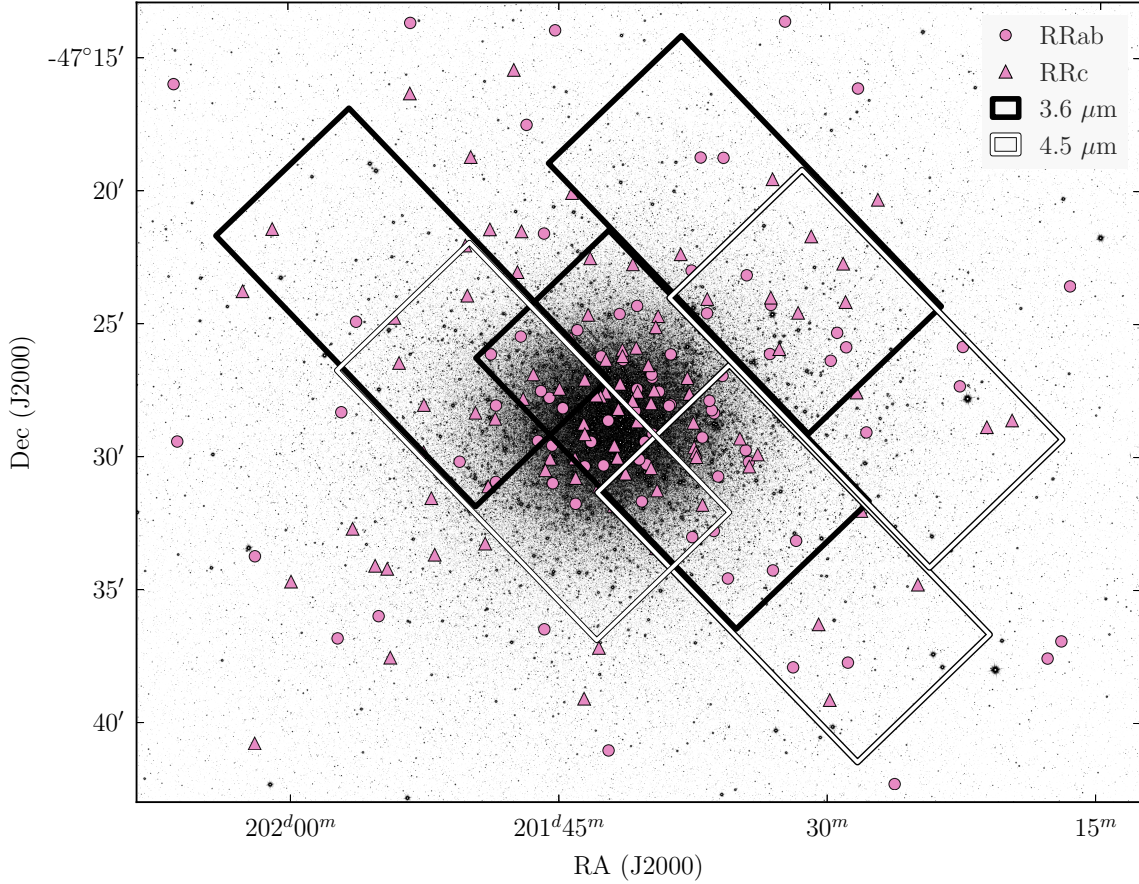


**Figure 1.** A  $K_s$ -band image of  $\omega$  Cen from the FourStar camera, overlaid with a catalog of RRL from Kaluzny et al. (2004) and footprints of the *Spitzer* IRAC fields. Here the circular points are RRab's and the triangular points are RRC's; we adopt this convention throughout the paper. The three black rectangle outlines are the IRAC field of view for each pointing in the  $3.6\ \mu\text{m}$  channel, and the white rectangle outlines are the same for  $4.5\ \mu\text{m}$ .

$5 \times 3$  (slightly overlapping) pointings (tiles) covered a  $50 \times 30$  arcminute field of view centered on  $\omega$  Cen. Each tile consists of a 5 point dither pattern with a 5.8 second exposure time. Stacked mosaics of the entire field were made as well as individual tiles using a customized pipeline for FourStar data. The purpose of the individual tiles is to provide photometry with better time resolution than the large mosaic.

PSF photometry of the tiles was performed using DAOPHOT and ALLFRAME (Stetson 1987, 1994). A PSF model was created for each epoch/tile/filter combination. A master star list for ALLFRAME was created from the final  $K_s$  mosaic and the multi-wavelength/epoch results were combined using DAOMATCH and DAOMASTER. Our final photometry is calibrated to the 2MASS standard system (Skrutskie et al. 2006).

### 2.3 Crowding

The primary limiting factor in the data is crowding. To assess crowding for individual RRLs, we compared the *Spitzer* images to the FourStar  $K_s$ -band image. The 0.159 arc-

sec/pixel resolution of the  $K_s$  band image compared to the 0.6 arcsec/pixel resolution of the IRAC images enabled us to more accurately determine which stars were significantly contaminated. 77 RRLs out of the original catalog of 192 (Kaluzny et al. 2004) were rejected due to crowding.

### 3 RESULTS

Our final photometry catalog, including magnitudes and uncertainties for  $JHK_s$ , [3.6], and [4.5], is presented in Table A1. **Note: this will not be an appendix in the final draft, we're just putting it there for now because it's huge.** The average magnitudes presented in Table A1 are flux averages, and the photometric uncertainties of the time series data are the error on the mean. GLOESS fitting Persson et al. (2004) was attempted on the light curves as done in previous CCHP works (e.g. Scowcroft 2011, Monson 2012, Rich 2014, Scowcroft 2016) [FIND REFS], but it was not found to improve results.

Our full, uncrowded RRL sample consists of 96 stars in



**Table 1.** Empirical mid-IR RRL period-luminosity relation coefficients for  $\omega$  Cen (Neeley et al. 2015), for relations of the form  $M = a + b \times (\log(P) + P_0)$  with intrinsic dispersion  $\sigma$ .

Band	Mode	$a$	$b$	$P_0$	$\sigma$
[3.6]	RRab	-0.558	-2.370	0.260	0.040
	RRc	-0.192	-2.658	0.550	0.079
[4.5]	RRab	-0.593	-2.355	0.260	0.045
	RRc	-0.240	-2.979	0.550	0.057

**Table 2.** Theoretical near-IR RRL period-luminosity relation coefficients for  $\omega$  Cen (Marconi et al. 2015), for relations of the form  $M = a + b \times \log P + c \times [\text{Fe}/\text{H}]$  with intrinsic dispersion  $\sigma$ .

Band	Mode	$a$	$b$	$c$	$\sigma$
$J$	RRab	-0.510	-1.980	0.170	0.060
	RRc	-1.070	-2.460	0.150	0.040
$H$	RRab	-0.760	-2.240	0.190	0.040
	RRc	-1.310	-2.700	0.160	0.020
$K_s$	RRab	-0.820	-2.270	0.180	0.030
	RRc	-1.370	-2.720	0.150	0.020

$J$  and  $H$ , 98 in  $K_s$ , 38 in [3.6], and 42 in [4.5]. For the PL fitting, detailed in the next section, we use only the stars for which we have photometry in all five bandpasses, ensuring that the same range of periods and metallicities are sampled for each wavelength. This reduces the possibility of biases being introduced by inconsistent RRL samples to the distance moduli we fit in Section 5. Our final RRL sample consists of 24 stars, or 12 in each pulsation mode.

#### 4 PERIOD-LUMINOSITY RELATIONS

We use the theoretical near-infrared PL relation parameters presented in Marconi et al. (2015) for the  $JHK_s$  bands, and the empirical PL relation parameters derived from photometry of RRLs in the globular cluster M4 (NGC 6121) from Neeley et al. (2015) for the IRAC bands. With the use of preexisting PL relation coefficients, the distance modulus becomes the only free parameter in our fit. We fit all distance moduli using an unweighted least-squares method, and fit the distance modulus to each pulsation mode in each wavelength separately.

For the mid-IR we use the PL relations from Neeley et al. (2015), as described in Table 1. These relations take the form

$$M = a + b \times (\log(P) + P_0) \quad (1)$$

where  $a$  and  $b$  are empirically derived coefficients and  $P_0$  is the absolute value of the logarithm of the mean period of the M4 RRL sample. We calculate the absolute PL zero-points from Neeley et al.'s apparent ones using Neeley et al.'s M4 distance modulus of  $\mu = 11.399$  mag.

The  $JHK_s$  RRL PL relations are described in Table 2. The relations take the form

$$M = a + b \times \log P + c \times [\text{Fe}/\text{H}] \quad (2)$$

where  $a$ ,  $b$ , and  $c$  are theoretically derived coefficients.

The theoretical PL relations for the near-IR have a

metallicity-dependent term; however, we do not have known metallicities for all RRL in our sample. We therefore use the average  $[\text{Fe}/\text{H}]$  of the RRLs for which there are known metallicities. Using spectroscopic metallicities from Sollima et al. (2006), we obtain an average  $[\text{Fe}/\text{H}]$  of  $-1.67$ .

#### 5 DISTANCE MODULI

The distance moduli derived from the PL fitting have not been corrected for reddening. We combine the uncorrected distance moduli from each bandpass to obtain a mean reddening value and reddening-corrected distance modulus. We fit the near-infrared reddening law from Cardelli et al. (1989) to the  $JHK_s$  data and the mid-infrared law from Indebetouw et al. (2005) to [3.6] and [4.5] simultaneously, assuming a ratio of total to selective absorption  $R_V = 3.1$ . The resulting fit is shown in Figure 3. We derive a true mean dereddened distance modulus of  $\langle\mu_0\rangle = 13.781 \pm 0.018$  with  $E(B-V) = 0.066 \pm 0.030$  using the weighted mean RRab + RRc distances. The individual uncorrected distance moduli  $\mu$ , corrected distance moduli  $\mu_0$ , and PL residuals are shown in Table 3.

It is apparent from Figure 3 that there are large discrepancies in the distance moduli in [3.6] and [4.5] for the two pulsation modes; these contribute to the relatively low  $E(B-V)$  value and high dereddened distance modulus. If we remove the RRc's and fit the extinction curve only to the RRab's, as shown in Figure 4, we obtain a better fit of all points to the extinction curve than when we use the mean. From these distance moduli we derive a true dereddened distance modulus of  $\langle\mu_0\rangle = 13.739 \pm 0.024$  with  $E(B-V) = 0.110 \pm 0.042$ , both of which are closer to accepted values (OTHER REFS) than the values derived from the weighted mean distance moduli. All individual corrected distance moduli from this fit are shown in Table 4.

Given the large errors in the [4.5] distances, we also fit the extinction curve to the  $JHK_s$  and [3.6] distances only, excluding [4.5] entirely; this was found to have a negligible effect on the final distance modulus and reddening for both the mean and RRab-only measurements.

#### 6 METALLICITY

Theoretical models suggest that the metallicity dependence of the RRL PL relation should decrease monotonically from the optical to the near-infrared (Bono et al. 2001; Catelan et al. 2004). Observational evidence corroborates this; previous investigations performed on WISE data suggest no obvious metallicity dependence in the mid-IR PL relations (Madore et al. 2013).

$\omega$  Cen is ideal for examining the RRL period-luminosity-metallicity relation, because **need source for canonical metallicity spread** A metallicity spread this wide is not found in any other Galactic globular cluster. One of the advantages of using globular clusters to calibrate PL coefficients is that all stars in a cluster can be considered to be at the same distance from Earth. We can therefore assume that any dispersion in the PL relation is a combination of the a) the intrinsic dispersion of the PL relation, b) the photometric uncertainties, and c) dispersion induced by

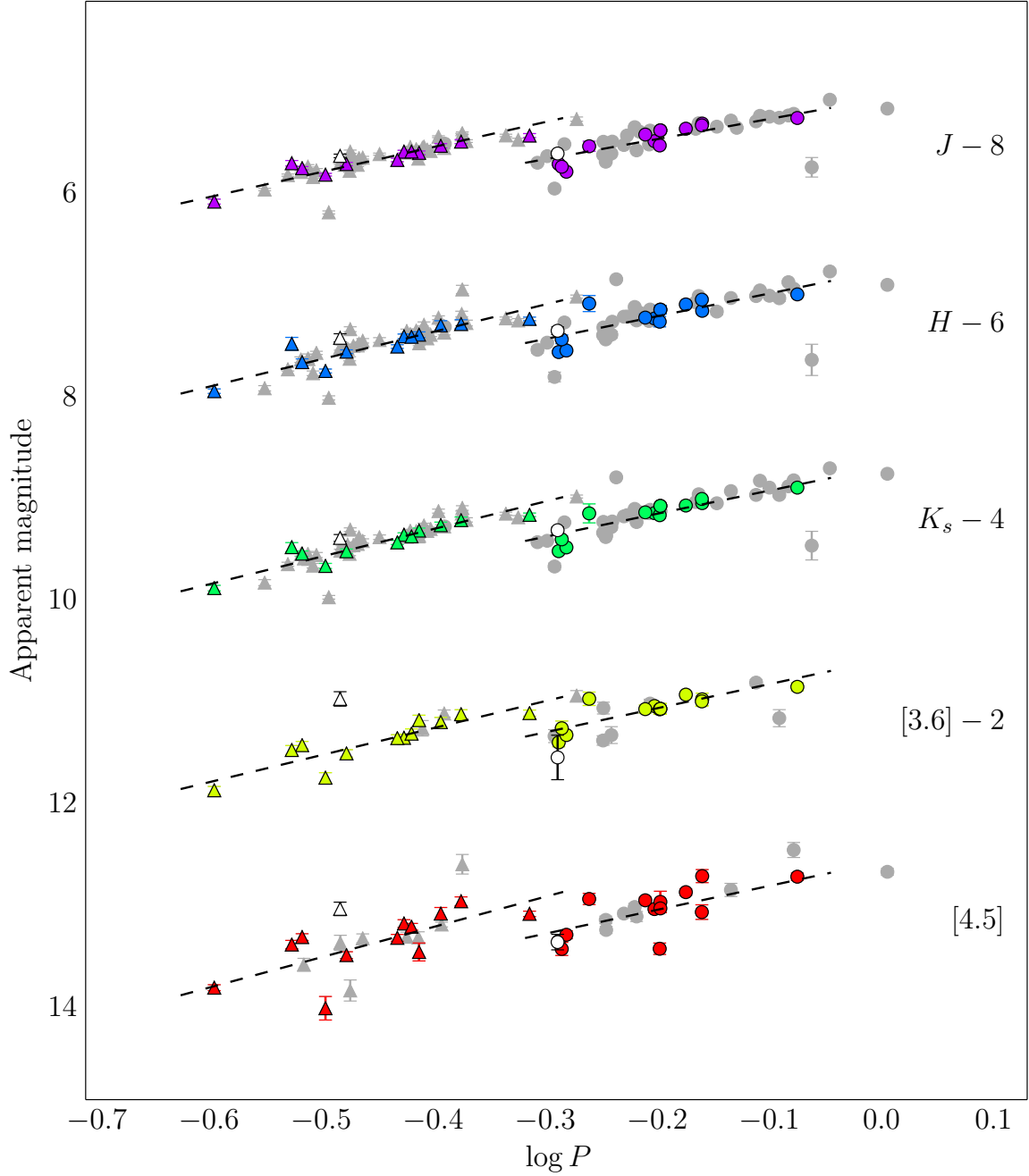


**Figure 2.** PL relations for  $JHK_s$ ,  $[3.6]$ , and  $[4.5]$  photometry assuming  $[\text{Fe}/\text{H}] = -1.567$ . Here circles represent RRAb stars, triangles represent RRCs, colored points are the final consistent sample, grey points are stars that did not appear in all bands, and the unfilled points are stars rejected from the final sample based on  $2\sigma$  clipping of the residuals of  $3.6\ \mu\text{m}$  vs. the residuals of  $H$  and  $K$ .

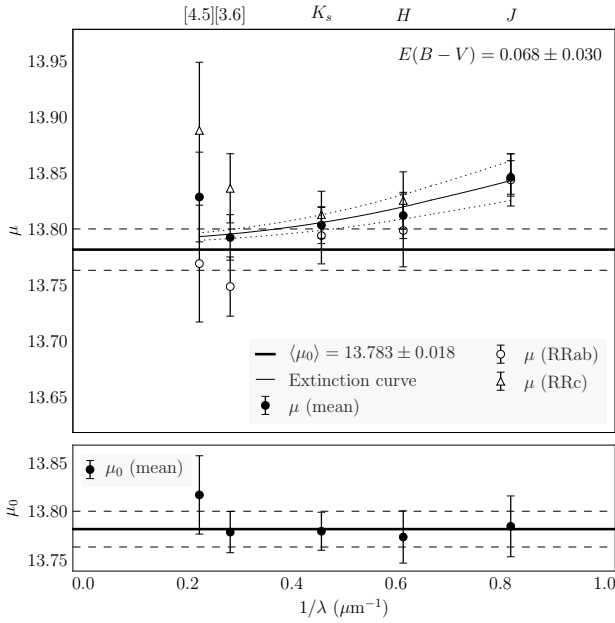
other complicating factors such as the spread in metallicity. Since we have measured the intrinsic dispersion of the RRL PL in  $[3.6]$  and  $[4.5]$  from the cluster M4 (Neeley et al. 2015) and our photometric uncertainties are well understood, the only unknown in this problem is the dispersion due to the spread in metallicity of the cluster.

We know from mid-IR spectra that a significant CO feature sits within the IRAC  $[4.5]$  filter. In the case of Cepheids, Monson et al. (2012) have shown that this has a significant

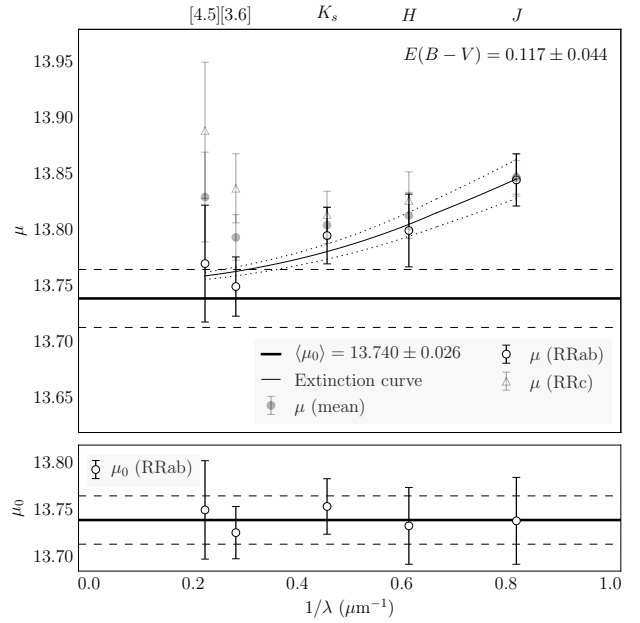
effect on the  $[4.5]$  magnitudes, and is metallicity dependent. However, this effect decreases with increasing temperatures, turning off completely above 6000 K where all the CO has been destroyed (Monson et al. 2012). As even the coolest RRL have temperatures over 6000 K (Iben 1971), we expect to see no such CO absorption in the  $[4.5]$  PL relation. If there are any other unanticipated metallicity effects for RRL, they must be smaller than the dispersion of the PL

**Table 3.** Uncorrected distance moduli  $\mu$ , corrected distance moduli  $\mu_0$ , and the PL dispersion  $\sigma$ . The corrected distance moduli  $\mu_0$  are equal to  $\mu - A_\lambda A_V$ , where  $A_V$  is derived from fitting the reddening laws to the mean distance moduli.

Band	$\mu$ , R Rab	$\mu$ , R Rc	$\mu$ , mean	$\mu_0$ , R Rab	$\mu_0$ , R Rc	$\mu_0$ , mean	$\sigma_{\text{PL}}$ , R Rab	$\sigma_{\text{PL}}$ , R Rc
<i>J</i>	$13.839 \pm 0.022$	$13.850 \pm 0.019$	$13.844 \pm 0.015$	$13.779 \pm 0.035$	$13.790 \pm 0.033$	$13.784 \pm 0.031$	0.077	0.063
<i>H</i>	$13.796 \pm 0.030$	$13.827 \pm 0.026$	$13.811 \pm 0.020$	$13.758 \pm 0.035$	$13.790 \pm 0.031$	$13.773 \pm 0.026$	0.108	0.085
<i>K_s</i>	$13.790 \pm 0.024$	$13.814 \pm 0.021$	$13.802 \pm 0.016$	$13.767 \pm 0.026$	$13.791 \pm 0.023$	$13.778 \pm 0.019$	0.084	0.070
[3.6]	$13.751 \pm 0.024$	$13.838 \pm 0.031$	$13.793 \pm 0.019$	$13.738 \pm 0.025$	$13.825 \pm 0.031$	$13.779 \pm 0.020$	0.088	0.102
[4.5]	$13.768 \pm 0.048$	$13.890 \pm 0.061$	$13.826 \pm 0.038$	$13.756 \pm 0.048$	$13.878 \pm 0.061$	$13.815 \pm 0.039$	0.173	0.202

**Figure 3.** Top: Uncorrected distance moduli for the final sample of *JHK<sub>s</sub>*, [3.6], and [4.5] photometry. Filled circles are the mean distance moduli using both R Rab and R Rc stars, open circles are the distance moduli using only R Rab stars, and open triangles are distance moduli using only R Rc stars. Here the NIR and MIR reddening laws are fit to the mean distance moduli. The solid and dashed horizontal lines are the mean corrected distance modulus and its  $1\sigma$  errors respectively. Bottom: reddening-corrected distance moduli and mean corrected distance modulus. Errors on the corrected distance moduli are the quadrature sum of the uncorrected distance moduli errors and the reddening error at the requisite wavelength.**Table 4.** Corrected distance moduli  $\mu_0$  using the  $A_V$  value derived from fitting the reddening laws to only the R Rab distance moduli.

Band	$\mu_0$ , R Rab	$\mu_0$ , R Rc	$\mu_0$ , mean
<i>J</i>	$13.739 \pm 0.044$	$13.750 \pm 0.043$	$13.744 \pm 0.041$
<i>H</i>	$13.733 \pm 0.039$	$13.764 \pm 0.035$	$13.748 \pm 0.031$
<i>K_s</i>	$13.751 \pm 0.028$	$13.775 \pm 0.026$	$13.763 \pm 0.022$
[3.6]	$13.729 \pm 0.026$	$13.815 \pm 0.032$	$13.770 \pm 0.021$
[4.5]	$13.749 \pm 0.049$	$13.871 \pm 0.061$	$13.807 \pm 0.039$

**Figure 4.** Same as Figure 3, with the reddening laws fit to the R Rab distances only instead of the mean.

relations themselves, but we must still perform empirical tests to search for such effects.

### 6.1 Metallicity Contribution to the Overall Dispersion

We can place an upper limit on the contribution of metallicity to the measured PL dispersion by combining the probability distributions of the known intrinsic PL width and the scatter induced by photometric error and comparing the result to the observed distribution of  $\omega$  Cen PL residuals. The following description of the process uses the R Rab PL relation in [3.6] as the example case; we apply this method to both pulsation modes in both IRAC filters, with results presented in Table 5. We model the intrinsic scatter as a uniform distribution with an area of 1 and full  $12\sigma$  width of  $\sqrt{12}$  times the intrinsic PL width (see Table 1),  $\sqrt{12} \times 0.040 = 0.139$  mag and the photometric uncertainties as a unit area Gaussian distribution with a standard deviation of the mean photometric error in the sample,  $\sigma = 0.048$  mag. We model the probability distribution of the observed PL residuals as a unit area Gaussian centered at zero with a scale of the standard deviation of the residuals,  $\sigma = 0.088$

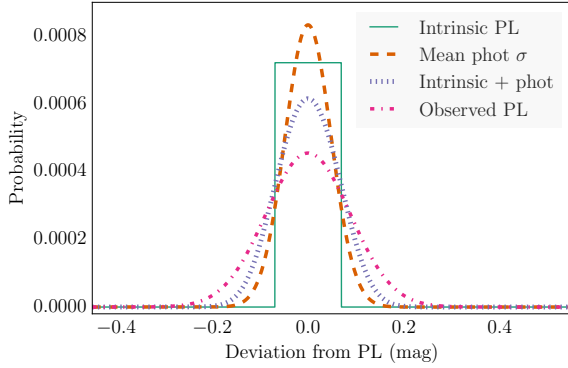


**Figure 5.** Probability distributions for components of PL scatter for RRab's in [3.6], with intrinsic width in green, photometric error in orange, the combination thereof in purple, and the observed distribution in pink.

**Table 5.** The standard deviation of the observed spread of the PL residuals  $\sigma_{\text{observed}}$  ( $\sigma_{\text{PL}}$  in Table 3) and its components:  $\sigma_{\text{intrinsic}}$  ( $\sigma$  in Table 1),  $\sigma_{\text{phot}}$ , and  $\sigma_{[\text{Fe}/\text{H}]}$  for all IRAC PL relations.

Band	Mode	$\sigma_{\text{observed}}$	$\sigma_{\text{intrinsic}}$	$\sigma_{\text{phot}}$	$\sigma_{[\text{Fe}/\text{H}]}$
[3.6]	RRab	0.088	0.040	0.048	0.061
[3.6]	RRc	0.102	0.079	0.041	0.046
[4.5]	RRab	0.173	0.045	0.046	0.160
[4.5]	RRc	0.202	0.057	0.048	0.187

mag. These models are shown in Figure 5, as well as the convolution of the intrinsic scatter and photometric error distributions.

To constrain the contribution of metallicity to the observed scatter, we model the metallicity-induced scatter as another Gaussian centered at zero. To find the standard deviation of this model, we convolve the metallicity distribution with the previous convolution of the intrinsic width and photometric error distributions, and minimize the difference between that and the observed distribution. For RRab's in [3.6], we find the standard deviation of the model metallicity distribution to be  $\sigma = 0.061$ , as shown in Figure 6. The results for all IRAC PLs are in Table 5.

We use these measurements to assess the  $\gamma$  parameter for  $\omega$  Cen, where

$$\gamma = \frac{\delta \text{mag}}{\delta [\text{Fe}/\text{H}]}, \quad (3)$$

similar to  $\gamma$  used to quantify the effect of metallicity on the zero-point of the Cepheid PL relation (Kennicutt et al. 1998; Scowcroft et al. 2009). Here we calculate  $\gamma$  by dividing the standard deviation of the metallicity component of the PL scatter by the standard deviation of the metallicity values; the results for each PL are shown in Table 6. We use all available metallicity values for each pulsation mode when taking the standard deviation, as we do not have metallicity values for all stars in our sample, although the ones we do have represent the overall metallicity distributions fairly well (see Figure 7) considering the small sample sizes.

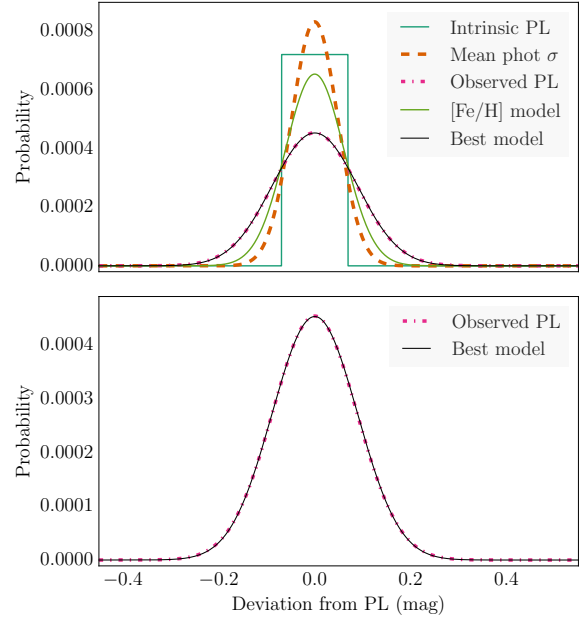


**Figure 6.** Top: Intrinsic, photometric error, and observed PL relations for RRab's in [3.6] as in Figure 5, as well as the scaled metallicity distribution and best model (convolution of intrinsic, photometric, and metallicity distributions). Bottom: only the observed and model distributions for easier comparison.

**Table 6.** Metallicity standard deviations and  $\gamma$  values.

Band	Mode	$\sigma_{[\text{Fe}/\text{H}]\text{spect}}$	$\sigma_{[\text{Fe}/\text{H}]\text{phot}}$	$\gamma_{\text{spect}}$	$\gamma_{\text{phot}}$
[3.6]	RRab	0.250	0.254	0.244	0.240
[3.6]	RRc	0.132	0.243	0.349	0.189
[4.5]	RRab	0.250	0.254	0.642	0.632
[4.5]	RRc	0.132	0.243	1.420	0.771

## 6.2 PL Residuals and Individual Metallicities

$\omega$  Cen is unique in that we can also take a second approach to establishing the metallicity effect on the RRL PL relation. As it is such an interesting system,  $\omega$  Cen is extremely well studied and many of its RRL have spectroscopic or photometric metallicities in the literature (e.g. Sollima et al. 2006; Rey et al. 2000).

If there is any correlation between  $[\text{Fe}/\text{H}]$  and the PL residuals, we expect it to be a linear one, consistent with the theoretical metallicity terms in the  $JHK_s$  PL relations,  $c \times [\text{Fe}/\text{H}]$ . We fit a relation of the form

$$\Delta \text{mag} = \gamma \times [\text{Fe}/\text{H}] + d \quad (4)$$

to the [3.6] and [4.5] PL residuals and metallicity values for stars with known individual metallicity values, as shown in Figure 8. By this metric we find that although the scatter in the [3.6] and [4.5] PL relations is higher for  $\omega$  Cen than it is for M4 (Neeley et al. 2015; Braga et al. 2015), there is currently not enough evidence to ascribe it to metallicity alone. When we examine  $[\text{Fe}/\text{H}]$  vs. the residuals of each PL relation,  $\gamma$  is within  $1\sigma$  of zero for all fits, indicating

that there is no significant metallicity dependence in the PL residuals.

## 7 DISCUSSION

While we find high upper bounds on the contribution of metallicity to the PL scatter in the IRAC passbands, particularly [4.5], it is unlikely that this scatter is due to metallicity alone. Gratton et al. (1986) and Lee (1991) demonstrate that RRL luminosity is dependent on the horizontal branch morphology as well as metallicity, and that  $\omega$  Cen contains RRL in multiple evolutionary states.

Results from the *GAIA* mission (Lindgren & Perryman 1996) are expected to improve the overall characterization of the RRL PL relation dramatically. Trigonometric parallaxes and spectrophotometric metallicities of Galactic RRLs from *GAIA* will increase the number of calibrators for the absolute RRL PL relations by an order of magnitude (Liu et al. 2012, **overview paper**). **something about omega cen parallaxes and metallicities too**

We also anticipate that the NIRC*am* instrument on *JWST* (Burriesci 2005; Gardner et al. 2006) will provide substantial improvements over IRAC for investigations of this nature. The NIRC*am* filters F356W and F444W will provide data in passbands comparable to IRAC's [3.6] and [4.5] at an order of magnitude higher resolution (0.065 arcsec/pixel), which will significantly decrease photometric error due to crowding and therefore allow us to obtain data for all known RRLs in  $\omega$  Cen.

## 8 CONCLUSIONS

We derive a true mean dereddened distance modulus for  $\omega$  Cen of  $\langle\mu_0\rangle = 13.739 \pm 0.024$  with reddening  $E(B - V) = 0.110 \pm 0.042$  using distance moduli derived from RR*ab* PL relations in *JHK<sub>s</sub>*, [3.6], and [4.5]. Using the mean of RR*ab* and RR*c* distance moduli in the same passbands, we derive a true mean dereddened distance modulus of  $\langle\mu_0\rangle = 13.781 \pm 0.018$  with reddening  $E(B - V) = 0.066 \pm 0.030$ . The RR*ab* results are closer to literature values.

We also constrain the contribution of metallicity, quantified as  $\gamma = \Delta\text{mag}/\Delta[\text{Fe}/\text{H}]$ , to the scatter of the  $\omega$  Cen PL relations by subtracting the variances of the intrinsic scatter and photometric error from the observed PL variance and taking the square root of the result, and dividing that by the standard deviation of the distribution of metallicity values. We also

## ACKNOWLEDGEMENTS

We thank Eric Persson for his many contributions to this project.

This work is based on observations made with the Spitzer Space Telescope, which is operated by the Jet Propulsion Laboratory, California Institute of Technology under a contract with NASA. Support for this work was provided by NASA through an award issued by JPL/Caltech.

This work was also supported in part by the Claremont-Carnegie Astrophysics Research Program.

This publication makes use of data products from the

Two Micron All Sky Survey, which is a joint project of the University of Massachusetts and the Infrared Processing and Analysis Center/California Institute of Technology, funded by the National Aeronautics and Space Administration and the National Science Foundation.

This research has made use of the NASA/IPAC Extragalactic Database (NED), which is operated by the Jet Propulsion Laboratory, California Institute of Technology, under contract with the National Aeronautics and Space Administration.

## REFERENCES

- Benedict G. F., et al., 2011, *AJ*, **142**, 187  
 Bono G., Caputo F., Castellani V., Marconi M., Storm J., 2001, *MNRAS*, **326**, 1183  
 Braga V. F., et al., 2015, *ApJ*, **799**, 165  
 Burriesci L. G., 2005, in Heaney J. B., Burriesci L. G., eds, Society of Photo-Optical Instrumentation Engineers (SPIE) Conference Series Vol. 5904, Cryogenic Optical Systems and Instruments XI. pp 21–29, doi:10.1117/12.613596  
 Cardelli J. A., Clayton G. C., Mathis J. S., 1989, *ApJ*, **345**, 245  
 Catelan M., Pritzl B. J., Smith H. A., 2004, *ApJS*, **154**, 633  
 Cusano F., et al., 2015, *ApJ*, **806**, 200  
 Efsthathiou G., 2014, *MNRAS*, **440**, 1138  
 Fazio G. G., et al., 2004, *ApJS*, **154**, 10  
 Freedman W. L., et al., 2011, *AJ*, **142**, 192  
 Freedman W., et al., 2012a, The Carnegie RR Lyrae Program, Spitzer Proposal  
 Freedman W. L., Madore B. F., Scowcroft V., Burns C., Monson A., Persson S. E., Seibert M., Rigby J., 2012b, *ApJ*, **758**, 24  
 Freeman K. C., Rodgers A. W., 1975, *ApJ*, **201**, L71  
 Gardner J. P., et al., 2006, *Space Sci. Rev.*, **123**, 485  
 Garofalo A., et al., 2013, *ApJ*, **767**, 62  
 Gratton R. G., Tornambe A., Ortolani S., 1986, *A&A*, **169**, 111  
 Iben Jr. I., 1971, *PASP*, **83**, 697  
 Indebetouw R., et al., 2005, *ApJ*, **619**, 931  
 Kains N., et al., 2015, *A&A*, **578**, A128  
 Kaluzny J., Olech A., Thompson I. B., Pych W., Krzemiński W., Schwarzenberg-Czerny A., 2004, *A&A*, **424**, 1101  
 Kennicutt Jr. R. C., et al., 1998, *ApJ*, **498**, 181  
 Lee Y.-W., 1991, *ApJ*, **373**, L43  
 Lindgren L., Perryman M. A. C., 1996, *A&AS*, **116**, 579  
 Liu C., Bailer-Jones C. A. L., Sordo R., Vallenari A., Borrachero R., Luri X., Sartoretti P., 2012, *MNRAS*, **426**, 2463  
 Longmore A. J., Fernley J. A., Jameson R. F., 1986, *MNRAS*, **220**, 279  
 Madore B. F., Freedman W. L., 1991, *PASP*, **103**, 933  
 Madore B. F., et al., 2013, *ApJ*, **776**, 135  
 Makovoz D., Roby T., Khan I., Booth H., 2006, in Society of Photo-Optical Instrumentation Engineers (SPIE) Conference Series. p. 62740C, doi:10.1117/12.672536  
 Marconi M., et al., 2015, *ApJ*, **808**, 50  
 Monson A. J., Freedman W. L., Madore B. F., Persson S. E., Scowcroft V., Seibert M., Rigby J. R., 2012, *ApJ*, **759**, 146  
 Navarrete C., et al., 2015, *A&A*, **577**, A99  
 Neeley J. R., et al., 2015, *ApJ*, **808**, 11  
 Ordoñez A. J., Yang S.-C., Sarajedini A., 2014, *ApJ*, **786**, 147  
 Persson S. E., Madore B. F., Krzemiński W., Freedman W. L., Roth M., Murphy D. C., 2004, *AJ*, **128**, 2239  
 Persson S. E., et al., 2013, *PASP*, **125**, 654  
 Planck Collaboration et al., 2015, preprint, (arXiv:1502.01589)  
 Reach W. T., et al., 2005, *PASP*, **117**, 978  
 Rey S.-C., Lee Y.-W., Joo J.-M., Walker A., Baird S., 2000, *AJ*, **119**, 1824  
 Riess A. G., et al., 2011, *ApJ*, **730**, 119



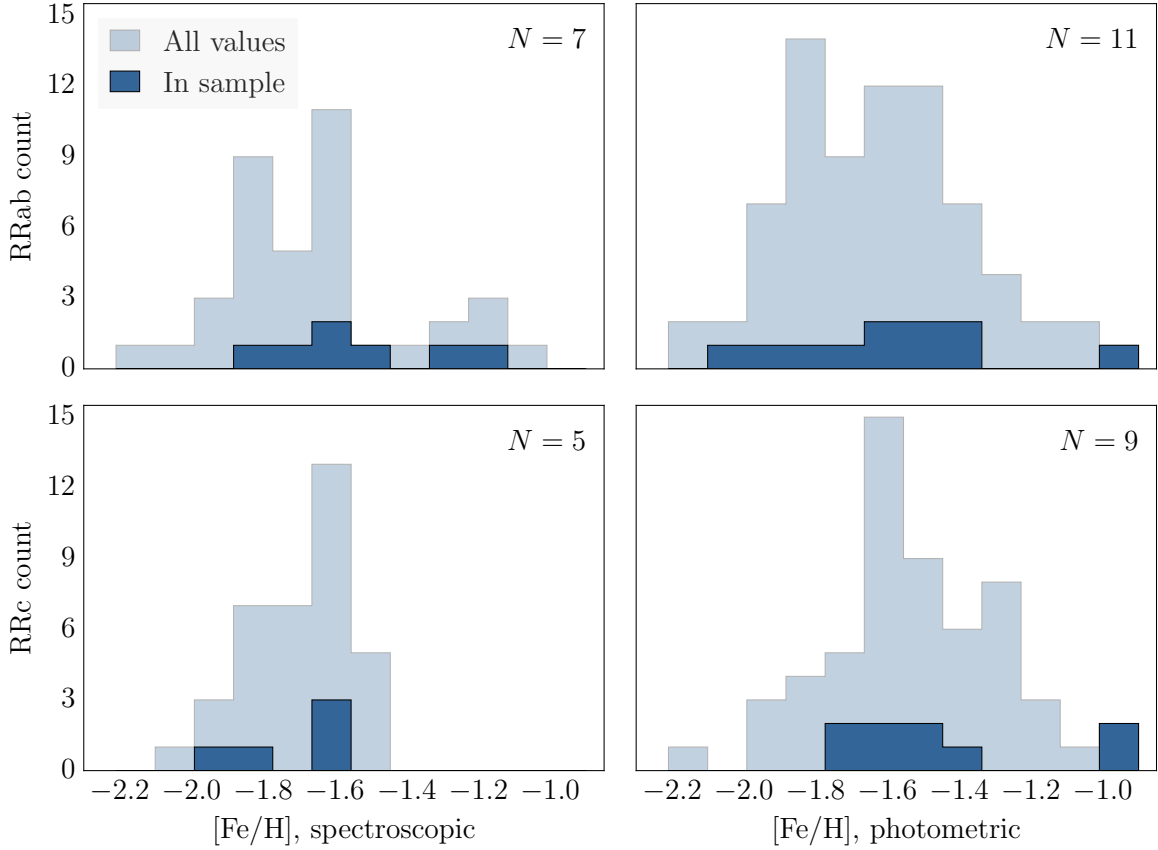


**Figure 7.** Histograms of spectroscopic (Sollima et al. 2006, right column) and photometric (Rey et al. 2000, left column)  $[Fe/H]$  values for RRAb (top row) and RRC (bottom row). The light blue histograms represent all known metallicity values for each type, and the dark blue are the metallicity values in our final RRL sample. The number  $N$  at the top right corner of each subplot is the number of stars in our final sample that have known metallicity values for the given type and metallicity catalog.

- Rigault M., et al., 2015, [ApJ](#), 802, 20  
 Scowcroft V., Bersier D., Mould J. R., Wood P. R., 2009, [MNRAS](#), 396, 1287  
 Scowcroft V., Freedman W. L., Madore B. F., Monson A. J., Persson S. E., Seibert M., Rigby J. R., Sturch L., 2011, [ApJ](#), 743, 76  
 Scowcroft V., Freedman W. L., Madore B. F., Monson A., Persson S. E., Rich J., Seibert M., Rigby J. R., 2016, [ApJ](#), 816, 49  
 Skrutskie M. F., et al., 2006, [AJ](#), 131, 1163  
 Sollima A., Borissova J., Catelan M., Smith H. A., Minniti D., Cacciari C., Ferraro F. R., 2006, [ApJ](#), 640, L43  
 Stetson P. B., 1987, [PASP](#), 99, 191  
 Stetson P. B., 1994, [PASP](#), 106, 250  
 Villanova S., et al., 2007, [ApJ](#), 663, 296  
 Villanova S., Geisler D., Gratton R. G., Cassisi S., 2014, [ApJ](#), 791, 107

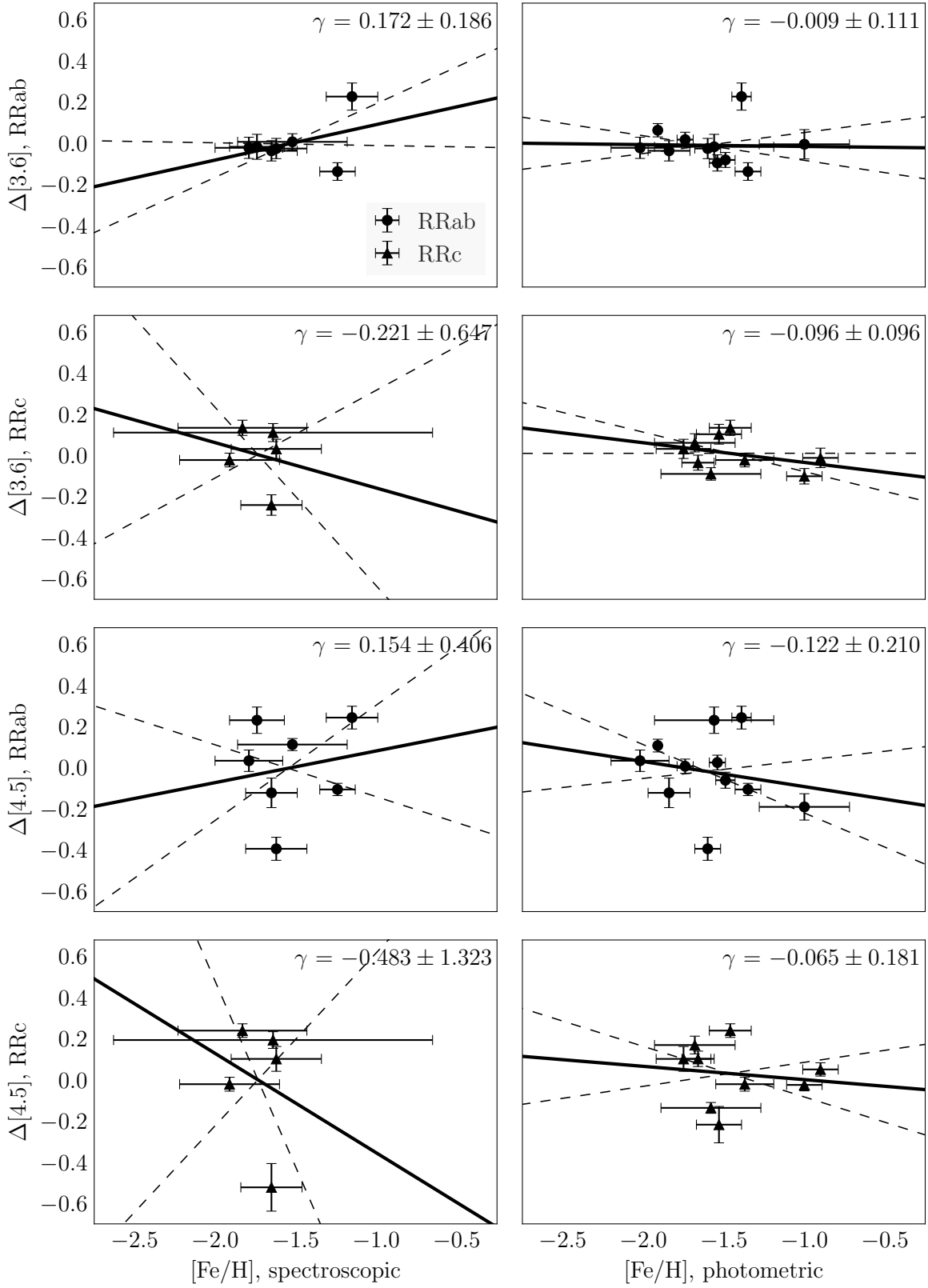


**Figure 8.** Photometric (Rey et al. 2000) and spectroscopic (Sollima et al. 2006) [Fe/H] values vs. period-luminosity residuals for RRab and RRc in [3.6] and [4.5]. Solid lines are the line of best fit with slope  $\gamma$ , and dashed lines are the  $1\sigma$  confidence intervals. The  $\gamma$  parameter from equation 4 in the top right corner of each subplot. All  $\gamma$  values are consistent with zero.

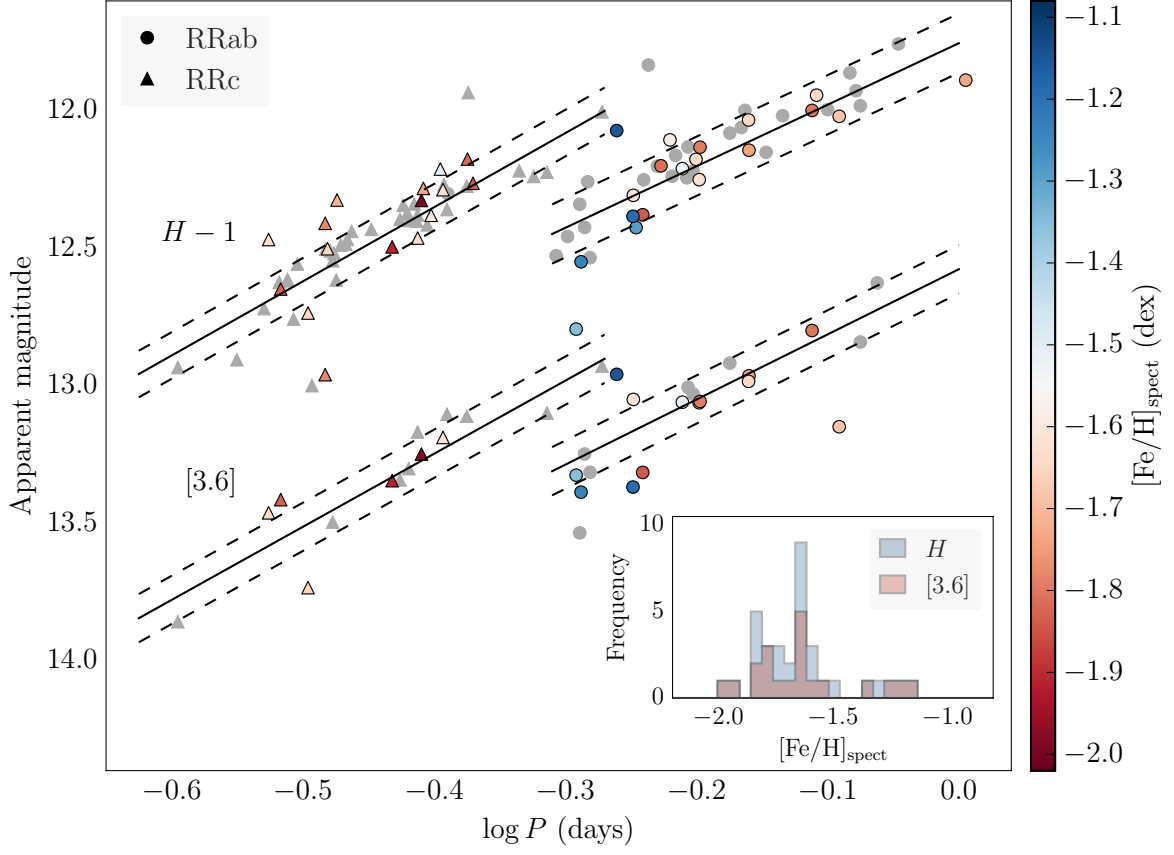


**Figure 9.** The  $H$ -band PL relation with fundamentalized RRC periods, with color indicating spectroscopic (Sollima et al. 2006, top) and photometric (Rey et al. 2000, bottom) metallicity values. Gray points have no known metallicity values.

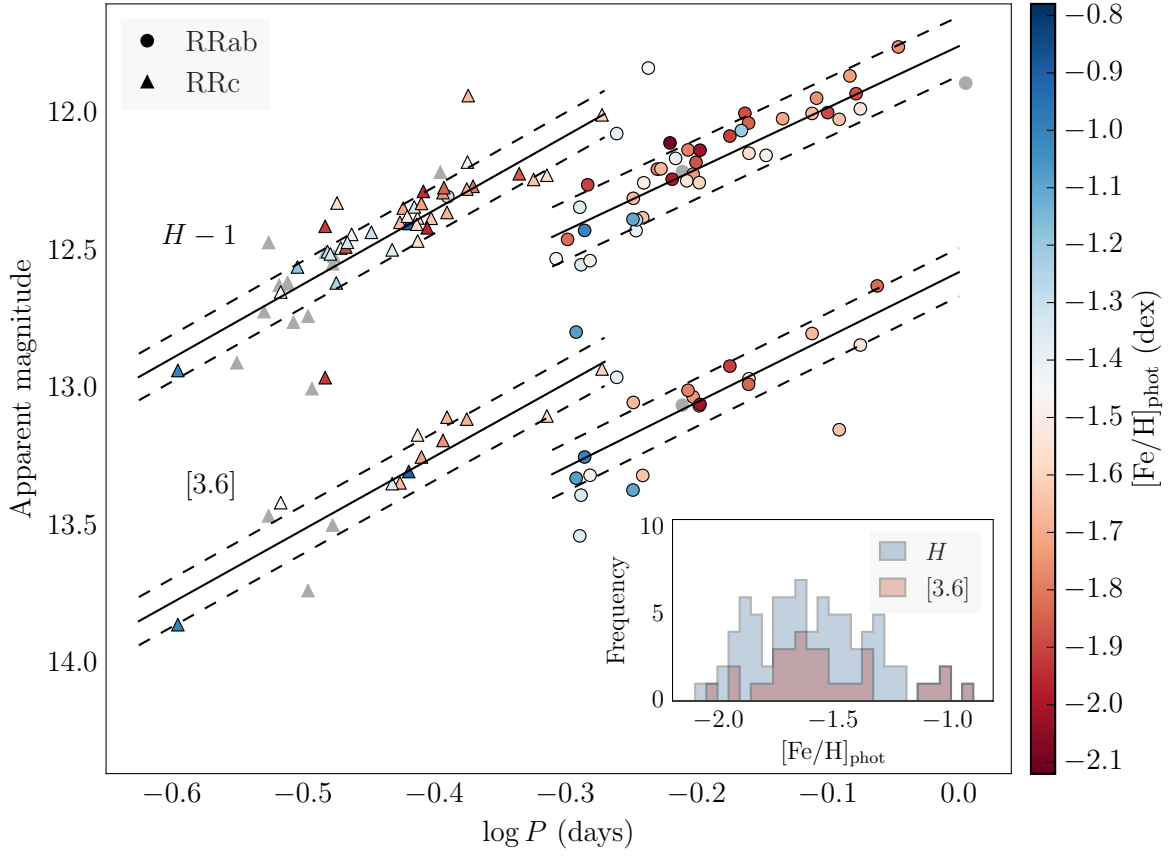


**Figure 10.** The  $H$ -band PL relation with fundamentalized RRC periods, with color indicating spectroscopic (Sollima et al. 2006, top) and photometric (Rey et al. 2000, bottom) metallicity values. Gray points have no known metallicity values.



**APPENDIX A: RRL PHOTOMETRY**

Table A1: Parameters for 99 RRLs in  $\omega$  Cen. First five columns are star ID, right ascension and declination, pulsation mode, and period in days from [Kaluzny et al. \(2004\)](#). Columns 6 through 11 are  $JHK_s$  apparent magnitudes and errors from FourStar data. Columns 12 through 17 are  $3.6\ \mu\text{m}$  and  $4.5\ \mu\text{m}$  apparent magnitudes, errors, and PL residuals ( $\Delta[3.6]$  and  $\Delta[4.5]$ ) from IRAC data. Columns 18-21 are photometric ([Fe/H], p) and spectroscopic ([Fe/H], s) metallicities and errors from [Rey et al. \(2000\)](#) and [Sollima et al. \(2006\)](#) respectively.

ID	RA (J2000)	Dec (J2000)	Mode	$P$ (days)	$J$	$\sigma_J$	$H$	$\sigma_H$	$K_s$	$\sigma_{K_s}$	[3.6]	$\sigma_{[3.6]}$	$\Delta[3.6]$	[4.5]	$\sigma_{[4.5]}$	$\Delta[4.5]$	[Fe/H], p	$\sigma_{[\text{Fe}/\text{H}]}, \text{p}$	[Fe/H], s	$\sigma_{[\text{Fe}/\text{H}]}, \text{s}$
3	13:25:56.15	-47:25:53.8	RRab	0.841	13.247	0.017	12.982	0.018	12.882	0.017	12.841	0.039	-0.087	12.708	0.036	0.035	-1.540	0.050	—	—
4	13:26:12.93	-47:24:18.8	RRab	0.627	13.475	0.016	13.219	0.021	13.133	0.020	13.030	0.036	0.026	13.026	0.035	0.016	-1.740	0.050	—	—
5	13:26:18.33	-47:23:12.4	RRab	0.515	13.700	0.017	13.549	0.020	13.507	0.027	13.387	0.043	-0.129	13.340	0.030	-0.096	-1.350	0.080	-1.240	0.110
7	13:27:00.90	-47:14:00.5	RRab	0.713	13.333	0.009	13.151	0.031	13.036	0.018	—	—	—	—	—	—	-1.460	0.080	—	—
8	13:27:48.45	-47:28:20.3	RRab	0.521	13.505	0.015	13.258	0.017	13.223	0.014	—	—	—	—	—	—	-1.910	0.280	—	—
9	13:25:59.58	-47:26:24.0	RRab	0.523	13.776	0.017	13.534	0.021	13.470	0.016	13.315	0.036	-0.072	13.279	0.039	-0.051	-1.490	0.060	—	—
10	13:26:06.99	-47:24:36.6	RRc	0.375	13.579	0.014	13.395	0.023	13.345	0.019	13.342	0.037	-0.026	13.168	0.037	0.112	-1.660	0.100	—	—
11	13:26:30.59	-47:23:01.6	RRab	0.565	13.481	0.014	13.307	0.028	13.219	0.025	13.050	0.058	—	—	—	—	-1.670	0.130	-1.610	0.220
12	13:26:27.21	-47:24:06.2	RRc	0.387	13.590	0.018	13.379	0.028	13.305	0.025	13.168	0.048	0.112	13.448	0.088	-0.208	-1.530	0.140	—	—
13	13:25:58.18	-47:25:21.6	RRab	0.669	13.353	0.019	13.081	0.022	13.058	0.017	12.918	0.032	0.072	12.860	0.031	0.117	-1.910	0.000	—	—
14	13:25:59.74	-47:39:09.6	RRc	0.377	13.588	0.011	13.343	0.020	13.365	0.016	—	—	—	13.299	0.045	—	-1.710	0.130	—	—
15	13:26:27.11	-47:24:38.0	RRab	0.811	13.245	0.018	13.020	0.031	12.954	0.025	13.149	0.084	—	—	—	—	-1.640	0.390	-1.680	0.180
16	13:27:37.69	-47:37:34.8	RRc	0.330	13.680	0.015	13.502	0.022	13.437	0.018	—	—	—	—	—	—	-1.290	0.080	-1.650	0.460
18	13:27:45.11	-47:24:56.6	RRab	0.622	13.371	0.010	13.131	0.024	13.100	0.016	13.006	0.043	—	—	—	—	-1.780	0.280	—	—
20	13:27:14.05	-47:28:06.3	RRab	0.616	13.410	0.015	13.210	0.036	13.125	0.025	13.060	0.039	0.016	12.940	0.029	0.122	—	—	-1.520	0.340
21	13:26:11.17	-47:25:58.8	RRc	0.381	13.578	0.016	13.399	0.027	13.361	0.020	13.301	0.047	-0.003	13.200	0.032	0.061	-0.900	0.110	—	—
22	13:27:41.04	-47:34:07.6	RRc	0.396	13.572	0.012	13.380	0.016	13.288	0.017	—	—	—	—	—	—	-1.630	0.170	-1.600	0.990
23	13:26:46.50	-47:24:39.5	RRab	0.511	13.941	0.025	13.794	0.048	13.658	0.033	13.325	0.064	—	—	—	—	-1.080	0.140	-1.350	0.580
24	13:27:38.32	-47:34:14.5	RRc	0.462	13.419	0.012	13.218	0.014	13.138	0.014	—	—	—	—	—	—	-1.860	0.030	—	—
30	13:26:15.94	-47:29:56.0	RRc	0.404	13.521	0.021	13.287	0.046	13.251	0.030	13.188	0.047	0.041	13.071	0.060	0.112	-1.750	0.170	-1.620	0.280
32	13:27:03.32	-47:21:38.9	RRab	0.620	13.508	0.009	13.244	0.018	13.132	0.018	—	—	—	—	—	—	-1.530	0.160	—	—
33	13:25:51.60	-47:29:05.8	RRab	0.602	13.338	0.015	13.106	0.022	13.091	0.019	—	—	—	13.006	0.035	—	-2.090	0.230	-1.580	0.420
34	13:26:07.21	-47:33:10.4	RRab	0.734	13.273	0.014	13.018	0.014	12.916	0.013	—	—	—	12.838	0.065	—	-1.710	0.000	—	—
35	13:26:53.21	-47:22:34.7	RRc	0.387	13.586	0.012	13.463	0.024	13.356	0.023	—	—	—	—	—	—	-1.560	0.080	-1.630	0.360
36	13:27:10.11	-47:15:29.8	RRc	0.380	13.534	0.007	13.372	0.019	13.307	0.014	—	—	—	—	—	—	-1.490	0.230	—	—
38	13:27:03.30	-47:36:30.2	RRab	0.779	13.226	0.015	12.943	0.019	12.814	0.018	—	—	—	—	—	—	-1.750	0.180	-1.640	0.400
39	13:27:59.77	-47:34:42.3	RRc	0.393	13.560	0.009	13.415	0.014	13.308	0.014	—	—	—	—	—	—	-1.960	0.290	—	—
40	13:26:24.56	-47:30:46.2	RRab	0.634	13.517	0.022	13.250	0.051	13.153	0.033	13.062	0.049	-0.017	13.416	0.056	-0.385	-1.600	0.080	-1.620	0.190
44	13:26:22.39	-47:34:35.3	RRab	0.568	13.677	0.014	13.425	0.023	13.368	0.018	—	—	—	13.132	0.036	—	-1.400	0.120	-1.290	0.350
45	13:25:30.88	-47:27:21.0	RRab	0.589	13.513	0.015	13.201	0.015	13.164	0.014	—	—	—	13.070	0.028	—	-1.780	0.250	—	—
46	13:25:30.23	-47:25:51.8	RRab	0.687	13.299	0.016	12.998	0.017	12.947	0.014	—	—	—	—	—	—	-1.880	0.170	—	—
47	13:25:56.46	-47:24:12.0	RRc	0.485	13.420	0.020	13.223	0.018	13.150	0.018	13.099	0.030	-0.080	13.073	0.026	-0.126	-1.580	0.310	—	—
49	13:26:07.78	-47:37:55.5	RRab	0.605	13.566	0.012	13.238	0.019	13.220	0.016	—	—	—	13.099	0.049	—	-1.980	0.110	—	—
50	13:25:53.94	-47:27:35.8	RRc	0.386	13.647	0.014	13.402	0.015	13.362	0.014	—	—	—	13.305	0.056	—	-1.590	0.190	—	—
51	13:26:42.66	-47:24:21.4	RRab	0.574	13.597	0.014	13.378	0.033	13.270	0.029	13.315	0.083	—	—	—	—	-1.640	0.210	-1.840	0.230
54	13:26:23.54	-47:18:47.7	RRab	0.773	13.281	0.016	12.998	0.017	12.954	0.015	12.799	0.030	—	—	—	—	-1.660	0.120	-1.800	0.230
56	13:25:55.53	-47:37:44.1	RRab	0.568	13.643	0.009	13.386	0.022	13.353	0.017	—	—	—	13.232	0.035	—	-1.260	0.150	—	—
57	13:27:49.38	-47:36:50.5	RRab	0.794	13.234	0.015	12.995	0.018	12.882	0.014	—	—	—	—	—	—	-1.890	0.140	—	—
58	13:26:13.05	-47:24:03.0	RRc	0.370	13.660	0.017	13.495	0.018	13.421	0.021	13.345	0.033	-0.013	13.309	0.034	-0.011	-1.370	0.180	-1.910	0.310
59	13:26:18.43	-47:29:46.7	RRab	0.519	13.727	0.023	13.424	0.043	13.391	0.033	13.248	0.071	0.004	13.418	0.064	-0.181	-1.000	0.280	—	—
63	13:25:07.96	-47:36:54.1	RRab	0.826	13.223	0.017	12.862	0.017	12.869	0.012	—	—	—	—	—	—	-1.730	0.090	—	—
64	13:26:02.22	-47:36:19.2	RRc	0.344	13.638	0.013	13.438	0.022	13.407	0.022	—	—	—	13.314	0.044	—	-1.460	0.230	—	—
66	13:26:33.08	-47:22:25.2	RRc	0.407	13.542	0.011	13.359	0.022	13.264	0.020	13.103	0.035	—	—	—	—	-1.680	0.340	—	—
67	13:26:28.62	-47:18:46.9	RRab	0.564	13.610	0.014	13.384	0.016	13.326	0.015	13.368	0.047	—	—	—	—	-1.100	0.000	-1.190	0.230
68	13:26:12.80	-47:19:35.7	RRc	0.535	13.258	0.021	13.004	0.015	12.970	0.015	12.928	0.050	—	—	—	—	-1.600	0.010	—	—
69	13:25:11.02	-47:37:33.5	RRab	0.635	—	—	—	—	13.112	0.014	—	—	—	—	—	—	-1.520	0.140	—	—
70	13:27:27.76	-47:33:42.7	RRc	0.391	13.529	0.013	13.282	0.029	13.254	0.022	—	—	—	—	—	—	-1.940	0.150	-1.740	0.300
72	13:27:33.11	-47:16:22.9	RRc	0.385	13.554	0.010	13.339	0.017	13.311	0.014	—	—	—	—	—	—	-1.320	0.220	—	—
73	13:25:53.75	-47:16:10.8	RRab	0.575	13.480	0.018	13.251	0.017	13.215	0.016	—	—	—	—	—	—	-1.500	0.090	—	—
74	13:27:07.22	-47:17:33.9	RRab	0.503	13.622	0.008	13.457	0.016	13.405	0.015	—	—	—	—	—	—	-1.830	0.360	—	—
75	13:27:19.70	-47:18:46.5	RRc	0.422	13.410	0.011	13.175	0.028	13.137	0.025	—	—	—	—	—	—	-1.490	0.080	-1.820	0.990
76	13:26:57.23	-47:20:07.7	RRc	0.338	13.634	0.012	13.488	0.017	13.449	0.020	—	—	—	—	—	—	-1.450	0.130	—	—
77	13:27:20.89	-47:22:05.6	RRc	0.426	13.474	0.013	13.264	0.028	13.199	0.021	—	—	—	—	—	—	-1.810	0.000	-1.840	0.430

*Continued on next page*

Table A1 - *Continued from previous page*

ID	RA (J2000)	Dec (J2000)	Mode	$P$ (days)	$J$	$\sigma_J$	$H$	$\sigma_H$	$K_s$	$\sigma_{K_s}$	[3.6]	$\sigma_{[3.6]}$	$\Delta[3.6]$	[4.5]	$\sigma_{[4.5]}$	$\Delta[4.5]$	[Fe/H], p	$\sigma_{[\text{Fe}/\text{H}]}$ , p	[Fe/H], s	$\sigma_{[\text{Fe}/\text{H}]}$ , s
79	13:28:24.99	-47:29:25.2	RRab	0.608	13.382	0.010	13.162	0.016	13.123	0.015	—	—	—	—	—	—	-1.390	0.180	—	—
81	13:27:36.68	-47:24:48.3	RRc	0.389	13.542	0.013	13.326	0.033	13.286	0.025	13.248	0.076	—	—	—	—	-1.720	0.310	-1.990	0.430
82	13:27:35.61	-47:26:30.3	RRc	0.336	13.579	0.016	13.324	0.024	13.296	0.018	—	—	—	13.827	0.104	—	-1.560	0.200	-1.710	0.560
83	13:27:08.42	-47:21:34.1	RRc	0.357	13.603	0.010	13.431	0.024	13.370	0.022	—	—	—	—	—	—	-1.300	0.220	—	—
84	13:24:47.45	-47:29:56.5	RRab	0.580	—	—	12.833	0.017	12.781	0.016	—	—	—	—	—	—	-1.470	0.100	—	—
85	13:25:06.49	-47:23:34.0	RRab	0.743	13.344	0.011	—	—	—	—	—	—	—	—	—	—	-1.870	0.310	—	—
94	13:25:57.06	-47:22:46.1	RRc	0.254	14.070	0.024	13.934	0.022	13.870	0.027	13.858	0.038	-0.092	13.799	0.029	-0.014	-1.000	0.110	—	—
95	13:25:24.95	-47:28:53.2	RRc	0.405	13.497	0.015	13.269	0.017	13.264	0.017	—	—	—	13.178	0.024	—	-1.840	0.550	—	—
97	13:27:08.49	-47:25:30.9	RRab	0.692	13.302	0.010	13.143	0.029	13.034	0.022	12.964	0.061	-0.008	12.702	0.064	0.240	-1.560	0.370	-1.740	0.170
101	13:27:30.24	-47:29:51.0	RRc	0.341	13.708	0.016	13.484	0.030	13.436	0.023	—	—	—	—	—	—	-1.880	0.320	—	—
102	13:27:22.11	-47:30:12.3	RRab	0.691	13.320	0.012	13.033	0.022	12.993	0.020	12.984	0.049	-0.028	13.056	0.072	-0.113	-1.840	0.130	-1.650	0.160
103	13:27:14.29	-47:28:36.3	RRc	0.329	13.620	0.018	13.409	0.040	13.377	0.034	12.960	0.071	—	13.024	0.066	—	-1.920	0.110	-1.780	0.270
104	13:28:07.76	-47:33:44.9	RRab	0.867	13.732	0.096	13.626	0.154	13.452	0.141	—	—	—	—	—	—	-1.830	0.180	—	—
105	13:27:46.02	-47:32:43.9	RRc	0.335	13.768	0.014	13.615	0.020	13.533	0.018	—	—	—	—	—	—	-1.240	0.180	—	—
107	13:27:14.05	-47:30:57.9	RRab	0.514	13.597	0.017	13.340	0.038	13.301	0.030	13.535	0.219	—	13.351	0.076	—	-1.360	0.110	—	—
115	13:26:12.30	-47:34:17.5	RRab	0.630	13.401	0.012	13.176	0.017	13.103	0.013	—	—	—	—	—	—	-1.870	0.010	-1.640	0.320
117	13:26:19.91	-47:29:21.0	RRc	0.422	13.480	0.020	13.274	0.043	13.202	0.031	13.110	0.044	0.071	12.949	0.043	0.179	-1.680	0.250	—	—
120	13:26:25.52	-47:32:48.6	RRab	0.549	13.525	0.049	13.072	0.079	13.135	0.094	12.958	0.066	0.236	12.927	0.055	0.253	-1.390	0.060	-1.150	0.160
121	13:26:28.17	-47:31:50.5	RRc	0.304	13.741	0.016	13.648	0.033	13.531	0.026	13.414	0.037	0.144	13.302	0.033	0.249	-1.460	0.130	-1.830	0.400
122	13:26:30.31	-47:33:02.2	RRab	0.635	13.369	0.018	13.132	0.042	13.062	0.024	13.057	0.052	-0.013	12.987	0.052	0.043	-2.020	0.180	-1.790	0.210
123	13:26:51.17	-47:37:13.2	RRc	0.474	13.462	0.016	13.239	0.019	13.174	0.017	—	—	—	—	—	—	-1.640	0.010	—	—
124	13:26:54.49	-47:39:07.5	RRc	0.332	13.708	0.013	13.510	0.018	13.482	0.023	—	—	—	—	—	—	-1.330	0.230	—	—
125	13:26:48.92	-47:41:03.7	RRab	0.593	13.420	0.015	13.200	0.016	13.153	0.015	—	—	—	—	—	—	-1.670	0.220	-1.810	0.380
126	13:28:08.03	-47:40:46.7	RRc	0.342	13.642	0.011	13.467	0.017	13.370	0.016	—	—	—	—	—	—	-1.310	0.130	—	—
127	13:25:19.36	-47:28:37.6	RRc	0.305	—	—	—	—	13.579	0.018	—	—	—	13.573	0.063	—	-1.590	0.080	—	—
128	13:26:17.75	-47:30:13.0	RRab	0.835	13.207	0.018	12.927	0.032	12.810	0.020	—	—	—	12.445	0.074	—	-1.880	0.040	—	—
130	13:26:09.93	-47:13:40.0	RRab	0.493	13.688	0.021	13.527	0.032	13.418	0.025	—	—	—	—	—	—	-1.460	0.170	—	—
147	13:27:15.86	-47:31:09.2	RRc	0.423	13.397	0.012	12.934	0.041	13.083	0.022	—	—	—	12.585	0.096	—	-1.660	0.140	—	—
149	13:27:32.94	-47:13:43.6	RRab	0.683	13.354	0.015	13.061	0.035	13.024	0.024	—	—	—	—	—	—	-1.210	0.240	—	—
150	13:27:40.21	-47:36:00.1	RRab	0.899	13.068	0.019	12.757	0.025	12.692	0.018	—	—	—	—	—	—	-1.760	0.340	—	—
151	13:28:25.40	-47:16:00.2	RRab	0.408	13.501	0.013	13.301	0.020	13.265	0.016	—	—	—	—	—	—	-1.300	0.240	—	—
163	13:25:49.42	-47:20:21.5	RRc	0.313	13.763	0.019	13.557	0.016	13.545	0.025	—	—	—	—	—	—	-1.180	0.270	—	—
168	13:25:52.78	-47:32:02.9	RRc	0.321	14.176	0.015	14.000	0.020	13.960	0.018	—	—	—	—	—	—	—	—	—	—
169	13:27:20.47	-47:23:59.1	RRc	0.319	13.805	0.013	13.735	0.019	13.652	0.025	13.734	0.050	-0.232	14.001	0.116	-0.512	—	—	-1.650	0.190
184	13:27:28.50	-47:31:35.4	RRc	0.303	13.778	0.012	13.624	0.028	13.536	0.019	—	—	—	—	—	—	—	—	—	—
185	13:26:04.13	-47:21:45.0	RRc	0.333	13.701	0.016	13.545	0.018	13.508	0.023	13.496	0.036	-0.043	13.479	0.033	-0.046	—	—	—	—
261	13:27:15.41	-47:21:29.5	RRc	0.403	13.431	0.009	13.212	0.019	13.113	0.020	—	—	—	—	—	—	—	—	-1.500	0.350
263	13:26:13.13	-47:26:09.7	RRab	1.012	13.155	0.017	12.888	0.017	12.746	0.016	—	—	—	12.660	0.034	—	—	—	-1.730	0.190
274	13:26:43.73	-47:22:48.2	RRc	0.311	13.828	0.011	13.758	0.023	13.650	0.022	—	—	—	—	—	—	—	—	—	—
276	13:27:16.51	-47:33:17.6	RRc	0.308	13.727	0.021	13.614	0.046	13.533	0.024	—	—	—	—	—	—	—	—	—	—
280	13:27:09.33	-47:23:05.7	RRc	0.282	13.951	0.012	13.905	0.026	13.816	0.029	—	—	—	—	—	—	—	—	—	—
285	13:25:40.20	-47:34:48.4	RRc	0.329	13.687	0.017	13.504	0.027	13.503	0.015	—	—	—	13.358	0.074	—	—	—	—	—
288	13:28:10.32	-47:23:47.8	RRc	0.295	13.809	0.011	13.719	0.016	13.635	0.019	—	—	—	—	—	—	—	—	—	—
289	13:28:03.68	-47:21:27.9	RRc	0.308	13.743	0.013	13.618	0.015	13.584	0.022	—	—	—	—	—	—	—	—	—	—
291	13:26:38.52	-47:33:28.0	RRc	0.334	13.674	0.018	13.518	0.044	13.444	0.026	—	—	—	—	—	—	—	—	—	—
357	13:26:17.77	-47:30:23.4	RRc	0.298	13.692	0.027	13.468	0.064	13.468	0.045	13.462	0.044	0.120	13.375	0.041	0.204	—	—	-1.640	0.990

This paper has been typeset from a  $\text{\TeX/L\AA\TeX}$  file prepared by the author.